Microwave spectroscopy of high-L, $n = 9$ Rydberg levels of nickel: Polarizabilities and moments of the Ni^+ ion

Shannon Woods, Chris Smith, Julie Keele, and S. R. Lundeen
Department of Physics, Colorado State University, Fort Collins, Colorado 80523, USA
(Received 1 February 2013; published 20 February 2013)

The complete pattern of Rydberg binding energies of the 18 $n = 9$ levels of nickel with $L = 6$, 7, and 8 was measured using microwave plus resonant-excitation Stark-ionization spectroscopy. The measured pattern is consistent with the form predicted with the effective potential model, showing significant structure proportional to scalar products of tensor operators of order 0–4. The variation of the structure with L separates the various contributing terms and provides determinations of several properties of the Ni^+ core ion. These include the quadrupole moment, $Q = -0.469\,78(9)$ a.u., the hexadecapole moment, $\Pi = 0.36(5)$ a.u., the scalar and tensor dipole polarizabilities, $\alpha_{D,0} = 7.949(2)$ a.u., $\alpha_{D,2} = 0.905(12)$ a.u., the scalar quadrupole polarizability, $\alpha_{Q,0} = 55(8)$ a.u., the g value, $g_J = 1.257(14)$, and the vector hyperpolarizability, $\beta_{D,1} = 0.454(24)$ a.u.

DOI: 10.1103/PhysRevA.87.022511 PACS number(s): 32.10.Dk, 32.30.Bv

I. INTRODUCTION

The pattern of binding energies of nonpenetrating, high-L Rydberg electrons in atoms and ions can be related to the properties of the core ion that control the ion's long-range interactions with the Rydberg electron, properties such as polarizabilities and permanent moments. If these interactions were absent, leaving only the dominant Coulomb force, these high-L levels would be degenerate except for small relativistic effects. The presence of permanent electric and magnetic moments and electric polarizabilities in the core ion lead to changes in the Rydberg electron's binding energy that produce characteristic binding-energy patterns. Measurement of these patterns can be used to determine the core properties responsible for them. In effect, the captive Rydberg electron acts as a sensitive probe of properties of the positively charged core ion that are difficult to measure for neutral atoms [1].

Understanding the long-range interactions of atoms and ions is important in many applications. For example, two of the most significant properties controlling these interactions are the dipole polarizability and the quadrupole moment. The dipole polarizability characterizes the deformability of an atom or ion in response to electric fields and is thus a very basic dynamic property of an atom. It figures in many applications ranging from Van der Waals interactions between cold atoms [2] to blackbody radiation frequency shifts of optical clocks [3] to parameterization of chemical interactions involving actinide and lanthanide ions [4], just to name a few. The electric quadrupole moment of an atom is the lowest nonzero electric moment of an atom other than total charge. It characterizes the first deviation from pure Coulomb interaction potential with other atoms or ions and also describes the atom's interaction with external electric-field gradients. One recent application is the description of frequency shifts of optical clocks based on monovalent ions such as Ca^+ due to electric-field gradients acting on the trapped ions [5]. These and other atomic properties controlling these interactions can, of course, be calculated, but the calculations are challenging, and the opportunity to test them in specific cases can provide valuable guidance and increased confidence. The measurements provided by study of high-L Rydberg systems are among the most precise tests yet achieved.

Spectroscopic studies of high-L Rydberg levels are relatively rare because these levels are not normally observed with standard absorption and emission spectroscopy. One special technique that allows observation and measurement of these states is the resonant excitation Stark ionization spectroscopy (RESIS) method [1], in which these levels are observed by upwards excitation, followed by Stark ionization of the excited level. This method circumvents the restrictive angular momentum selection rules that prevent observation of high-L levels in excitation from low-lying, low-angular-momentum levels since there are always excitation channels open even for very high angular-momentum states.

One recent RESIS study explored the structure of $n = 9$ levels of the nickel atom with $L \geqslant 5$ [6]. Since the ground state of the Ni^+ ion is a $^2D_{5/2}$ level, the pattern of high-L Rydberg binding energies in nickel is very complex, with six energy levels for each value of Rydberg orbital angular momentum. A theoretical framework for interpreting the observed structure and extracting values of the permanent moments and polarizabilities of the Ni^+ core was recently derived by the method of adiabatic expansion [7,8]. This motivated the present study, which improves the precision of the spectroscopic observations by using the RESIS plus microwave method, a double-resonance method in which selective optical RESIS excitation is used to detect direct microwave transitions between Rydberg levels of common n.

The high-L Rydberg levels bound to the $^2D_{5/2}$ ground state of Ni^+ can be characterized by their principal and angular-momentum quantum numbers, n and L, and by the vector sum of L and the core angular momentum J_c, $\vec{K} = \vec{L} + \vec{J}_c$. We denote them by nL_K, with L given in spectroscopic notation, I, K, L, for $L = 6, 7, 8$. The intermediate quantum number K adequately describes the Rydberg fine structure pattern, which is approximately the expectation value of an effective potential given by

$$\langle V_{\rm eff}\rangle = A_0 + A_1(\vec{L}\cdot\vec{J}_c) + A_2\left(\frac{\langle X^{[2]}(J_c)\cdot C^{[2]}(\hat{r})\rangle}{\left(\begin{smallmatrix} J_c & 2 & J_c \\ -J_c & 0 & J_c\end{smallmatrix}\right)}\right) + A_3(\langle X^{[3]}(J_c)\cdot T^{[3]}(\hat{r})\rangle) + A_4\left(\frac{\langle X^{[4]}(J_c)\cdot C^{[4]}(\hat{r})\rangle}{\left(\begin{smallmatrix} J_c & 4 & J_c \\ -J_c & 0 & J_c\end{smallmatrix}\right)}\right), \quad (1)$$

where the coefficients of each tensor product order are expressed in terms of radial expectation values of the hydrogenic Rydberg electron and properties of the Ni^+ core [7]. The second-, third-, and fourth-rank tensors in the space of the ion core, $X^{[2]}$, $X^{[3]}$, and $X^{[4]}$, are unit tensors; i.e., they have unit reduced matrix elements. The second- and fourth-rank tensor operators in the space of the Rydberg electron, $C^{[2]}$ and $C^{[4]}$, are standard spherical tensor operators, and $\hat{r}$ denotes the angular position of the Rydberg electron. The third-rank tensor operator in the space of the Rydberg electron, $T^{[3]}$, is defined by

$$T^{[3]} \equiv [C^{[2]}(\hat{r}) \otimes \vec{L}]^{[3]}.$$

Each tensor order is associated with a unique pattern of level energies within the nL manifold, and the coefficients A_i which measure the contributions of each order can be extracted from measurements and used to determine the properties of the core responsible for the long-range interactions with the Rydberg electron.

A much smaller structure due to the Rydberg electron spin splits each nL_K level into two levels with $J = K \pm 1/2$. This spin splitting is partially resolved in some of the microwave resonances observed in this study. It is described by the spin Hamiltonian

$$H_{S_R} = \frac{1}{2}\alpha^2 \frac{1}{r^3}[\vec{L} \cdot \vec{S}_R + g_J \vec{J}_c \cdot (1 - 3\hat{r}\hat{r}) \cdot \vec{S}_R], \qquad (2)$$

where α is the fine structure constant and g_J is the g factor of the $^2D_{5/2}$ ground state.

II. EXPERIMENT

Figure 1 is a schematic diagram of the apparatus used for this study. It differs from that used for the optical RESIS study [6] by the addition of a second laser interaction region and a region where a microwave electric field can be applied to the Rydberg beam. Another difference is a more efficient source of Ni^+ ions. In place of the Colutron ion source used in reference [6] a radio-frequency (rf) ion source manufactured by Beam Imaging Systems [9] is used. This source produces Ni^+ beams by sputtering from a nickel electrode within a rf-excited argon plasma. Typical charged beam intensities, extracted at 9.5 keV were about 30 nA. After extraction, the beam is focused by an einzel lens and passed through a $\vec{v} \times \vec{B}$ filter to select the $^{58}Ni^+$ ion. The beam then passes through a Rb $9F$ Rydberg target [10], where a small fraction ($\sim$1%) of the beam captures an electron to form a beam of neutral Ni Rydberg atoms. Immediately afterwards, a strong longitudinal electric field reflects any un-neutralized ions and Stark ionizes any Rydberg levels formed in states with $n > 15$. The remaining Rydberg beam then passes through the sequence of laser and microwave interaction regions. In both laser regions, the atoms encounter a cw CO_2 laser, Doppler tuned by adjusting the angle of intersection with the Rydberg beam so that it is resonant with a transition upwards from $n = 9$ to $n = 19$ or 20. Typical transitions are listed in Table II of Ref. [6]. The first laser region depletes the population of a specific $n = 9$ Rydberg fine structure level, e.g., the $9K_{4.5}$ level, ensuring a population difference with another $n = 9$ level, e.g., the $9L_{5.5}$ level. The microwave field, encountered next, is tuned to drive the transition between these two levels, replenishing the population of the previously depleted level. If this succeeds, the second laser interaction region, tuned to excite the same transition as the first, will excite more atoms to the $n = 19$ or 20 level. After passing through the second laser interaction region, the Rydberg beam enters a strong electric field that completely ionizes all $n = 19$ or 20 levels and deflects the resulting ions into a channel electron multiplier (CEM). The microwave resonance is revealed by measuring the component of the CEM current synchronous with chopping of the microwave field, with both lasers unchopped. A typical resonance signal is shown in Fig. 2.

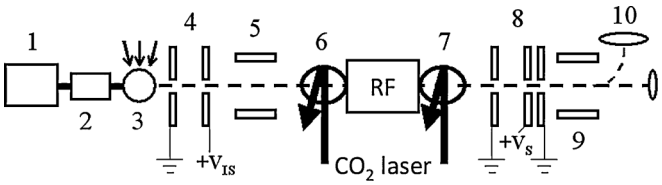

FIG. 1. Experimental apparatus schematic for the microwave RESIS technique of this experiment. A beam of Ni^+ ions is produced in the ion source at (1). The beam then enters the focusing/beam selection region at (2), where a $\vec{v} \times \vec{B}$ filter selects the $^{58}Ni^+$ beam and an einzel lens focuses the beam. At (3) a fraction of the ions capture an electron from the Rydberg target (RT), forming a beam of neutral Ni Rydberg atoms. The Rydberg target consists of a thermal beam of Rb stepwise excited by three cw diode lasers to the $9F$ level. The initial stripper at (4) Stark ionizes all Rydberg levels with $n > 15$ and reflects the resulting ions along with any remaining un-neutralized ions. Both laser interaction regions (LIRs) at (6) and (7) are tuned to excite the beam from a specific Rydberg level in a lower n to a higher n' (e.g., $9 \rightarrow 19$ or $10 \rightarrow 30$), while the rf region between the LIRs drives a transition connecting the specific Rydberg level excited by the lasers to another level of the same lower n. In the detector, the final stripper at (8) Stark ionizes states with the upper n' which are then deflected by the field at (9) into the channel electron multiplier (CEM) at (10).

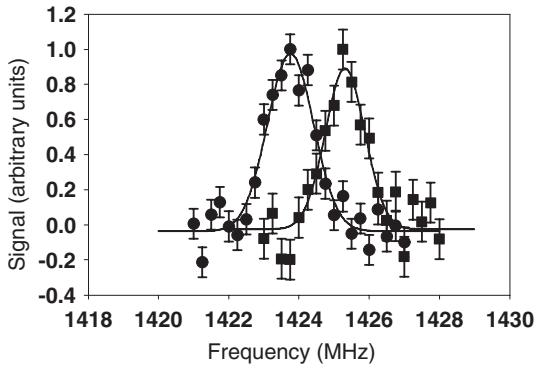

FIG. 2. An example microwave resonance, the $9K_{5.5}$-$9L_{6.5}$ transition. Data from both directions of microwave propagation relative to the Rydberg beam velocity are shown. Each was fit to a superposition of two signals offset from the spinless position by calculated Rydberg spin splittings, and the fitted line centers from both directions were averaged to remove the Doppler shift.

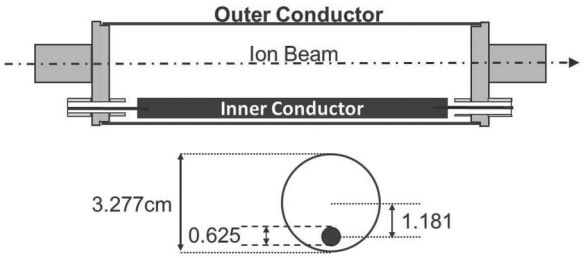

FIG. 3. Radio-frequency region diagram giving its basic appearance (top) and showing the dimensions (in cm) of the inner and outer conductors (bottom). The length of the region is 12.7 cm.

The microwave interaction region is illustrated in Fig. 3. It is an eccentric 50Ω TEM transmission line, in which the microwave field propagates either parallel or antiparallel to the Rydberg beam. Resonance signals are obtained with both directions of propagation and the line centers averaged to remove the associated Doppler shifts. The resonance linewidths, controlled by the transit time through the 12.7-cm-long microwave field region, were about 1.4 MHz. Since this partially resolves some of the splittings due to Rydberg electron spin, the lines were fit to a superposition of two lines offset from the spinless interval by the calculated spin splitting with relative weights given by the statistical weights of the lower L levels. In the cases of largest spin splitting, the calculated splittings matched the observations well. The resulting measurements of "spinless" intervals are shown in Table I.

TABLE I. Measured intervals separating high-$Ln = 9$ Rydberg levels of Ni. The given intervals represent the intervals separating Rydberg spin-averaged level positions. The measurement errors include statistical errors from the data fits, as well as estimated uncertainties due to stray electric-field corrections. Transitions marked by asterisks are two-photon transitions. Column 3 shows the net Stark shift correction, including both dc Stark shifts due to stray fields and, in the case of two-photon transitions, the ac Stark shift. All values are in MHz.

Interval	No.	Net Stark correction	Result
$I_{4.5}$-$K_{5.5}$	2	0.000(4)	3295.471(31)
$I_{5.5}$-$K_{6.5}$	2	0.000(5)	1109.996(24)
$I_{5.5}$-$K_{5.5}$	2	0.000(1)	2718.039(50)
$I_{6.5}$-$K_{7.5}$	2	0.000(1)	118.556(30)
$I_{7.5}$-$K_{8.5}$	3	0.041(58)	517.278(61)
$I_{7.5}$-$K_{7.5}$	3	0.013(18)	2345.468(32)
$I_{8.5}$-$K_{9.5}$	2	0.002(2)	4136.91(10)
$K_{4.5}$-$L_{5.5}$	3	0.000(2)	2901.667(28)
$K_{5.5}$-$l_{6.5}$	2	0.000(1)	1424.529(22)
$K_{5.5}$-$L_{5.5}$	2	0.000(1)	2127.303(39)
$K_{6.5}$-$L_{7.5}$	2	0.000(3)	179.680(21)
$K_{7.5}$-$L_{8.5}$	3	0.000(19)	444.435(16)
$K_{7.5}$-$L_{7.5}$	3	0.000(10)	1416.489(34)
$K_{9.5}$-$L_{10.5}$	2	−0.004(5)	2121.23(6)
$K_{9.5}$-$L_{9.5}$	2	−0.15(5)	6656.69(15)
$I_{3.5}$-$L_{5.5}$(*)	3	−0.010(2)	8598.584(28)
$I_{7.5}$-$L_{9.5}$(*)	2	−0.230(66)	532.340(76)

The only appreciable systematic corrections in these measurements involve the possibility of Stark shifts due to stray dc electric fields within the microwave interaction region and the ac Stark shifts of the two transitions observed by two-photon resonance. Possible dc fields were monitored with periodic observation of the $10H_{4.5}$-$10I_{5.5}$ transition in argon whose Stark shift rate and zero-field position has been established in previous work [11]. Since the ion source producing Ni^+ beams also contained an Ar discharge, it was a simple matter to switch between ion beams for these observations. Repeated observations over the course of the nickel measurements indicated that any stray fields present were very small, $\leqslant 0.1$ V/cm. Corrections and uncertainties associated with these shifts are shown in column 3 of Table I. ac Stark shifts are inherent to the two transitions listed last in Table I, which were observed using two-photon resonances. The relative ac Stark shift rate of these two transitions is easily calculated once the approximate level pattern is known. The absolute shift rate of the most sensitive transition, the $9I_{7.5}$-$9L_{9.5}$, was measured with 20% precision and used to calculate corrections to both transitions. These corrections are also included in column 3 of Table I.

The 17 measured intervals completely define the relative positions of all 18 Rydberg levels in $n = 9$ with $L = 6$, 7, and 8. The inferred positions are shown in column 2 of Table II. The uncertainties shown are derived from propagating the uncertainties in the interval measurements. Figure 4 illustrates the measured pattern of energy levels. Notice that the full span of the pattern is about 16 GHz. By comparison, the nearest other n level is about 8000 GHz away, indicating that all of these high-L levels have quantum defects $\delta < 0.001$.

III. CORE PROPERTIES

It is expected that this pattern is approximately the expectation value of an effective potential that describes the long-range interactions between the core ion and the Rydberg electron [7]. The first few terms of this potential are given by

$$V_{\rm eff}((J_c,L;K),r) = -\frac{1}{2}\frac{\alpha_{D,0}}{r^4} - \left(\frac{Q}{r^3}+\frac{1}{2}\frac{\alpha_{D,2}}{r^4}\right)\frac{X^{[2]}(J_c)\bullet C^{[2]}(\hat{r})}{\begin{pmatrix} J_c & 2 & J_c \\ -J_c & 0 & J_c\end{pmatrix}}+\cdots. \quad (3)$$

Many additional terms of this potential are described in Ref. [7], but these first terms suffice to illustrate the principle. The term containing the core quadrupole moment Q is simply the first-order Coulomb perturbation energy in a system whose zeroth-order states are products of hydrogenic Rydberg electrons and a separate free ion core. The terms proportional to the scalar and tensor dipole polarizabilities, $\alpha_{D,0}$ and $\alpha_{D,2}$, are typical of most of the terms in the effective potential, which come from the second-order perturbation energy, manipulated by use of the so-called "adiabatic expansion" of the energy denominators that occur The expectation value of this extended effective potential, augmented by small relativistic corrections, provides a good approximate description of the Rydberg energy level pattern. One thing that is left out of this model, however, is the portion of the second-order perturbation energy that involves intermediate "Rydberg levels," levels where the

TABLE II. Positions of the $n = 9$, $L = 6, 7$, and 8 levels of nickel, as determined by the measured intervals given in Table I. Column 1 identifies the specific level, and column 2 gives its position. Since only relative positions can be determined in this way, the position of the $9I_{5.5}$ level is arbitrarily defined as zero. The energy level pattern is completely determined by the 17 measured intervals, but is not overdetermined. The uncertainties in the positions are determined by propagating the interval measurement errors. Columns 3 and 4 give the calculated contributions to the level positions from relativistic and second-order corrections. Column 5 shows the inferred position that can be attributed to the expectation value of the effective potential. Two uncertainties apply to the results in column 5. The first is the statistical error from column 2. The second is the estimated uncertainty in the calculated second-order polarization energy shown in column 4. These two sources of uncertainty are treated differently in the subsequent analysis, as discussed in the text. All values are in MHz.

Level	Position	E_{rel}	$E^{[2]}$	$E^{[1]}$
$9I_{3.5}$	−13 443.926(69)	−16.945	−7.869(333)	−13 419.112
$9I_{4.5}$	−6013.510(59)	−16.945	8.082(693)	−6004.647
$9I_{5.5}$	0.000(50)*	−16.945	10.690(224)	6.255
$9I_{6.5}$	2824.721(55)	−16.945	2.567(219)	2839.099
$9I_{7.5}$	360.697(57)	−16.945	−10.138(126)	387.780
$9I_{8.5}$	−9900.563(204)	−16.945	−16.531(106)	−9867.087
$9K_{4.5}$	−7747.009(69)	−12.016	4.998(11)	−7739.991
$9K_{5.5}$	−2718.039(50)	−12.016	10.619(88)	−2716.642
$9K_{6.5}$	1109.996(24)	−12.016	7.761(116)	1114.251
$9K_{7.5}$	2706.165(47)	−12.016	0.859(7)	2717.322
$9K_{8.5}$	877.975(83)	−12.016	−2.803(14)	892.794
$9K_{9.5}$	−5763.653(177)	−12.016	−4.719(20)	−5746.918
$9L_{5.5}$	−4845.342(63)	−8.246	−1.811(4)	−4835.285
$9L_{6.5}$	−1293.510(55)	−8.246	0.104(5)	−1285.368
$9L_{7.5}$	1289.676(32)	−8.246	1.003(4)	1296.919
$9L_{8.5}$	2261.730(49)	−8.246	0.571(2)	2269.405
$9L_{9.5}$	893.037(95)	−8.246	−0.562(3)	901.845
$9L_{10.5}$	−3642.423(187)	−8.246	−1.336(5)	−3632.841

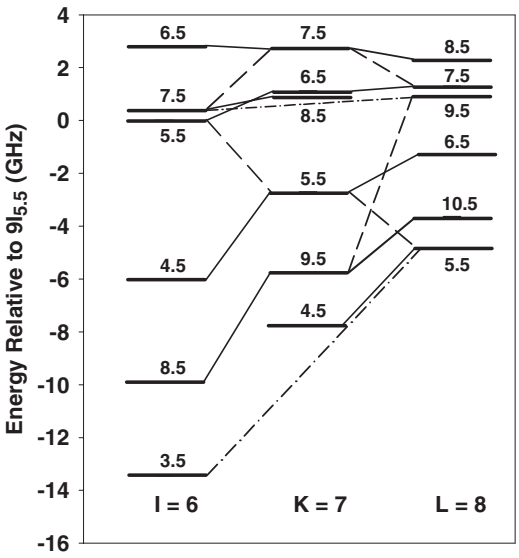

FIG. 4. Energy level diagram showing relative positions of the 18 $n = 9$ Rydberg levels of nickel with $L = 6$, 7, and 8, as determined from the measurements reported here. The spectroscopic notation for $L = 6, 7, 8$ (I, K, L) is indicated at the bottom of the graph. The values of the quantum number K are indicated for each level. The solid lines show transitions with $\Delta K = \Delta L$, the strongest transitions. The dashed lines show $\Delta K = 0$ transitions, and the dash-dotted lines show two-photon transitions. The position of the $9I_{5.5}$ level is arbitrarily assigned a zero value.

core ion is in its electronic ground state. In the case of Ni^+, this includes both the true ground state, the $^2D_{5/2}$, and an excited fine structure level, the $^2D_{3/2}$, at 1506.94 cm^{-1}. The Coulomb perturbations coupling different Rydberg levels bound to these two core states results in energy-level shifts that are not included in the expectation value of V_{eff}. These shifts can be very important for low-L levels, but they decrease rapidly with L, and if they are not too large can be described through the action of V_{eff} taken in second-order [7]. These shifts can be calculated once the core properties, such as Q and $\alpha_{D,0}$, that occur in V_{eff} are known, but since these properties are deduced here after the application of the $E^{[2]}$ corrections, it is necessary to iterate this process until stable results are obtained. Table II reports these calculated energy shifts, $E^{[2]}$, for the 18 Rydberg levels of this study. Notice that the largest calculated shifts are a few MHz, much smaller than the scale of the measured fine structure patterns. In view of the importance of the calculated $E^{[2]}$'s in the analysis, more details of these calculations are given in the Appendix.

In order to use the measured fine structure pattern to extract measurements of the Ni^+ ion's properties, it is necessary to remove the two effects that prevent the pattern from representing the expectation value of V_{eff}. These are the second-order effects of V_{eff}, denoted as $E^{[2]}$ and shown in column 4 of Table II, and the p^4 relativistic contributions, shown in column 3 of Table II. Subtracting both from the measured level positions leads to the corrected level positions, labeled $E^{[1]}$ and shown in column 5 of Table II. The uncertainties in the calculated $E^{[2]}$'s are quite significant. For some of the levels, especially $L = 6$ levels, they are larger than the measurement uncertainties in the level positions. The quoted uncertainties in $E^{[2]}$'s are based on the convergence of the calculated contributions. Contributions proportional to Q^2, $Q\alpha$, and $\alpha\alpha$ have been included, having total inverse powers of 6, 7, and 8, respectively. The uncertainty is taken to be 1/2 the total calculated contribution from terms proportional to r^{-8} [12], excluding the contribution proportional to $(\alpha_{D,0})^2$, which was applied separately to the scalar structure coefficient, A_0, since it only affects this coefficient.

The first step towards extracting measurements of core properties is to decompose the corrected level pattern for each L state, column 5 of Table II, into the five tensor orders shown in Eq. (1), essentially fitting the positions to extract values of the coefficients A_i, for $i = 0$–4. These fits were carried out with a weighted least-squares fit, using the statistical uncertainties shown first in column 5 of Table II and expanding the parameter errors based on the fit χ^2. In addition, the fits were repeated after each position was augmented by the uncertainty in the calculated $E^{[2]}$ correction from column 4 of Table II, thus assuming that these errors are completely correlated between the several levels. The change in the best fit A_i's that resulted

TABLE III. Fitted values of the structure coefficients, A_i, for $n = 9$, $L = 6$, 7, and 8 levels of nickel. The two errors shown for each represent (1) the statistical error resulting from propagating interval measurement errors, expanded to reflect the quality of the fit, and (2) the error associated with the uncertainty in the $E^{[2]}$ correction, calculated by incrementing each $E^{[1]}$ position by the uncertainty in $E^{[2]}$ and refitting to note the change in each A_i. In most cases, the statistical errors dominate. The scalar structure factor, A_0, is the exception.

	$L = 6$	$L = 7$	$L = 8$
A_0	−3833.06(18,135)	−1664.34(9,22)	−748.077(63,43)
A_1	−0.502(22,15)	−0.5915(85,13)	−0.4682(55,1)
A_2	15 063.29(51,3)	9888.30(24,1)	6828.32(17,3)
A_3	−2.40(32,6)	−0.210(14,10)	0.101(93,1)
A_4	−9.22(11,10)	−3.012(58,10)	−1.200(44,1)

in these second fits was taken to be a systematic error in the A_i's. Table III reports the results of these fits and includes the two uncertainties assigned to each structure factor. Except for the scalar structure factors, A_0, the statistical errors dominate.

The variation of the structure factors, A_i, with L is what allows deduction of the various core properties. For example, the effective potential model predicts that the A_0 factor will be given by [7]

$$A_0 = -\tfrac{1}{2}[\alpha_{D,0}\langle r^{-4}\rangle_{nL} + (\alpha_{Q,0} - 6\beta_{D,0})\langle r^{-6}\rangle_{nL} + \cdots], \quad (4)$$

where $\alpha_{D,0}$ and $\alpha_{Q,0}$ are the scalar adiabatic dipole and quadrupole polarizabilities of Ni^+, and $\beta_{D,0}$ is a coefficient representing the first nonadiabatic correction to the dipole polarization energy. The radial expectation values refer to the hydrogenic zeroth-order Rydberg wave functions, so they are given by well-known analytic expressions [13], suitably corrected for the finite mass of the Ni^+ core ion. Since this experiment determines only the relative positions of the $n = 9$ levels, the inferred values of A_0 shown in Table III reflect the arbitrary choice of zero for the level positions. The difference of scalar structure factors, however, could be expected to obey

$$\Delta A_0 = -\tfrac{1}{2}(\alpha_{D,0}\Delta\langle r^{-4}\rangle + (\alpha_{Q,0} - 6\beta_{D,0})\Delta\langle r^{-6}\rangle + \cdots), \quad (5)$$

which suggests forming a linear plot where the y axis is the ratio of ΔA_0 to $\Delta\langle r^{-4}\rangle$ and the x axis is the ratio of $\Delta\langle r^{-6}\rangle$ to $\Delta\langle r^{-4}\rangle$. The coordinates for this plot are summarized in Table IV, and the plot is shown in Fig. 5. A least-squares fit finds the intercept of $-3.9747(12)$, corresponding to a scalar polarizability of $\alpha_{D,0} = 7.949(2)$ a.u. The fitted slope is $-0.7(1.4)$. In combination with an estimated value of $\beta_{D,0}$ of 8.9(1.2) a.u. [14], this allows a deduction of the scalar quadrupole polarizability,

$$\alpha_{Q,0} = 2 \times 0.7(1.4) + 6 \times 8.9(1.2) = 55(8) \text{ a.u.}$$

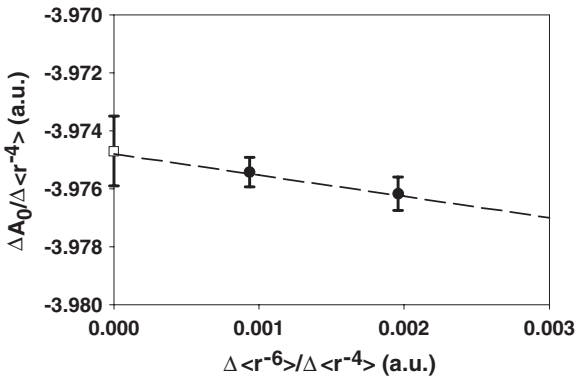

FIG. 5. Scaled values of the difference of the scalar structure factors, A_0, between adjacent L levels within the $n = 9$ level of nickel. The coordinates are given in Table IV. A linear least-squares fit determines the intercept, marked by the open point, and the slope. These can be related to the dipole and quadrupole scalar polarizabilities of Ni^+.

The vector structure factor A_1, the coefficient of $\vec{L} \bullet \vec{J}_c$ in Eq. (1), contains the effects of the magnetic moment of the core ion, as well as a contribution from the nonadiabatic dipole polarizability known as the "vector hyperpolarizability" [7,15]. The dependence on L is expected to be described by [7]

$$A_1 = -\frac{\alpha^2 g_J}{2}\langle r^{-3}\rangle_{nL} + \beta_{D,1}\langle r^{-6}\rangle_{nL} + \cdots . \quad (6)$$

This suggests scaling the measured structure factors by the expectation values of $\langle r^{-3}\rangle$ and plotting the ratio vs the ratio of $\langle r^{-6}\rangle$ to $\langle r^{-3}\rangle$. If higher order contributions are negligible, this should yield a straight line and separate the effect of the two terms. The coordinates of such a plot are shown in Table V, and the plot itself is shown in Fig. 6. Its fitted intercept and slope lead to the conclusions

$$g_J = 1.257(14), \quad \beta_{D,1} = 0.454(24) \text{ a.u.}$$

The second-order tensor structure factor, A_2, is primarily controlled by the permanent electric quadrupole moment of the Ni^+ ion, with smaller contributions from the tensor dipole polarizability, $\alpha_{D,2}$. Higher order contributions are expected from quadrupole and dipole-octupole polarizabilities and from nonadiabatic dipole polarizability. The form expected for this structure factor is [7]

$$A_2 = -Q\langle r^{-3}\rangle_{nL} - \frac{\alpha_{D,2}}{2}\langle r^{-4}\rangle_{nL} - \frac{(\alpha_{Q,2} - 6\beta_{D,2} + \alpha_{DO,2})}{2}\langle r^{-6}\rangle_{nL} + \cdots . \quad (7)$$

TABLE IV. Scaled values of the scalar structure factors, A_0, and the corresponding scaled differences of radial expectation values. Columns 5 and 6 represent the y and x coordinates of Fig. 5, respectively.

Interval	ΔA_0 (a.u.)	$\Delta\langle r^{-4}\rangle$ (a.u.)	$\Delta\langle r^{-6}\rangle$ (a.u.)	$\Delta A_0/\Delta\langle r^{-4}\rangle$	$\Delta\langle r^{-6}\rangle/\Delta\langle r^{-4}\rangle$
6-7	$-3.29609(47) \times 10^{-7}$	$8.289\,591 \times 10^{-8}$	1.6244×10^{-10}	−3.9762(6)	0.001 959 6
7-8	$-1.39256(18) \times 10^{-7}$	$3.502\,925 \times 10^{-8}$	0.3276×10^{-10}	−3.9754(5)	0.000 935 2

TABLE V. Scaled values of the vector structure factors, A_1, and the corresponding scaled radial expectation values.

L	A_1 (a.u.)	$\langle r^{-3}\rangle$ (a.u.)	$\langle r^{-6}\rangle$ (a.u.)	$A_1/\langle r^{-3}\rangle$	$\langle r^{-6}\rangle/\langle r^{-3}\rangle$
6	$-7.63(41)\times10^{-11}$	5.02455×10^{-6}	2.04213×10^{-10}	$-1.518(82)\times10^{-5}$	4.0643×10^{-5}
7	$-8.99(13)\times10^{-11}$	3.26596×10^{-6}	4.1771×10^{-11}	$-2.753(40)\times10^{-5}$	1.2790×10^{-5}
8	$-7.12(8)\times10^{-11}$	2.24135×10^{-6}	9.009×10^{-12}	$-3.175(37)\times10^{-5}$	4.0197×10^{-6}

This suggests scaling the measured structure factors by the expectation value of $\langle r^{-3}\rangle$ and plotting vs the ratio of $\langle r^{-4}\rangle$ to $\langle r^{-3}\rangle$. If only the first two terms in Eq. (7) are significant, this should be a linear plot. Figure 7 shows such a plot, using coordinates reported in Table VI. It is very close to linear. The slight curvature in the plot can be accounted for by including a term proportional to the ratio of $\langle r^{-6}\rangle$ to $\langle r^{-3}\rangle$. This results in a perfect fit of the three data points and determines the coefficients of the three inverse powers to be 0.469 78(9), $-0.453(6)$, and $-13.1(2.5)$. This implies values of the quadrupole moment and tensor polarizability,

$$Q = -0.46978(9)\ \text{a.u.}, \quad \alpha_{D,2} = 0.905(12)\ \text{a.u.}$$

The coefficient of $\langle r^{-6}\rangle$ is related to a combination of core properties, as indicated in Eq. (7).

The third-order tensor structure factor A_3 has contributions that are analogous to the vector structure factor A_1. The lowest order contribution is expected to be due to the permanent magnetic octupole moment of Ni^+. This term is likely to be quite small, as was the magnetic contribution to A_1. Its signature would be a coefficient of the third-order tensor product proportional to the inverse fifth power of the Rydberg radial coordinate. In the absence of specific theoretical predictions of this coefficient, we simply parameterize its possible contribution by a single constant, C_{M3}. As was the case for the vector structure, there are no adiabatic contributions to the third-order structure. However, nonadiabatic contributions to the quadrupole and dipole-octupole polarizabilities can contribute to the third-order structure. The form of the A_3 factor is expected to be [7]

$$A_3 = C_{M3}\langle r^{-5}\rangle_{nL} + (\beta_{Q,3} + \beta_{DO,3})\langle r^{-8}\rangle_{nL} + \cdots . \quad (8)$$

This suggests scaling the measured A_3 coefficients by the expectation value of $\langle r^{-5}\rangle$ and plotting the ratio vs the ratio between the expectation value of $\langle r^{-8}\rangle$ and $\langle r^{-5}\rangle$. These ratios are shown in Table VII and are plotted in Fig. 8. The data certainly conform to the expected pattern and fit well to a straight line. The fitted intercept gives

$$C_{M3} = 0.014(18)\ \text{a.u.},$$

which is consistent with zero. This is probably to be expected since the magnetic octupole contribution to the structure is likely to be very small. It would still be interesting to have a theoretical prediction of the expected magnetic octupole contribution, since it might be possible to measure it with this method. The fitted slope of the plot in Fig. 8 represents a quantity that is analogous to the vector hyperpolarizability, $\beta_{D,1}$, for the vector structure. It is a purely electric contribution to third-order tensor structure that is produced by the nonadiabatic response of the core to the electric field of the Rydberg electron. It could be called the "octupole hyperpolarizability,"

$$(\beta_{Q,3} + \beta_{DO,3}) = -1.1(3)\times10^3\text{a.u.}$$

The fourth-order tensor structure is due to the combined effects of the permanent hexadecapole moment of the Ni^+ core and fourth-order tensor quadrupole and dipole-octupole polarizabilities. The expected form of the fourth-order

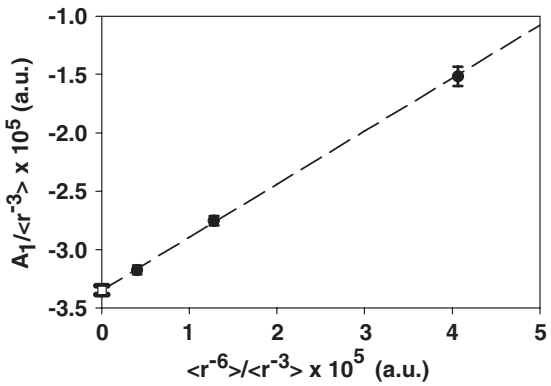

FIG. 6. Scaled values of the vector structure factor, A_1, from $n = 9$, $L = 6, 7, 8$ levels of nickel. The coordinates are taken from Table V. The intercept $[-3.348(38)\times10^{-5}]$ indicates the g value of Ni^+. The slope determines its vector hyperpolarizability. The open point marks the fitted intercept.

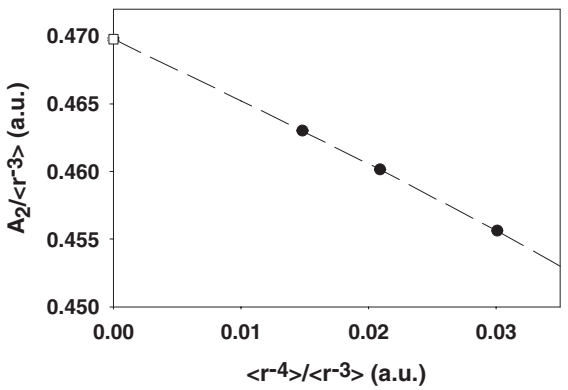

FIG. 7. Scaled values of the second-rank tensor structure factor, A_2, obtained from $n = 9$, $L = 6, 7, 8$ levels of nickel. The coordinates are taken from Table VI. The intercept, marked by the open point, and initial slope are related to the quadrupole moment and tensor dipole polarizability of Ni^+.

TABLE VI. Scaled values of the second-order tensor structure factors and the corresponding scaled radial expectation values. Expectation values of $\langle r^{-3}\rangle$ and $\langle r^{-6}\rangle$ are reported in Table V.

L	A_2 (a.u.)	$\langle r^{-4}\rangle$ (a.u.)	$A_2/\langle r^{-3}\rangle$	$\langle r^{-4}\rangle/\langle r^{-3}\rangle$	$\langle r^{-6}\rangle/\langle r^{-3}\rangle$
6	$2.289\,364(78) \times 10^{-6}$	$1.511\,300 \times 10^{-7}$	0.455 635(15)	0.030 0783	4.0642×10^{-5}
7	$1.502\,853(36) \times 10^{-6}$	$6.823\,405 \times 10^{-8}$	0.460 156(11)	0.020 8925	1.2790×10^{-5}
8	$1.037\,788(26) \times 10^{-6}$	$3.320\,480 \times 10^{-8}$	0.463 021(12)	0.014 8147	4.0197×10^{-6}

structure is

$$A_4 = -\Pi\langle r^{-5}\rangle_{nL} - \frac{(\alpha_{Q,4} + \alpha_{DO,4})}{2}\langle r^{-6}\rangle_{nL} + \cdots, \quad (9)$$

where Π is the hexadecapole moment. To separate the two contributions, A_4 is scaled by the expectation value of $\langle r^{-5}\rangle$ and plotted vs the ratio of $\langle r^{-6}\rangle$ to $\langle r^{-5}\rangle$. The relevant quantities are collected in Table VIII and plotted in Fig. 9. In this case, the data are a rather poor fit to a straight line. However, when the parameter errors are expanded to reflect the poor fit, the intercept is found to be $-0.36(5)$, as shown in Fig. 9. This corresponds to a hexadecapole moment of

$$\Pi = 0.36(5) \text{ a.u.}$$

The result is in agreement with the estimate obtained from the optical RESIS study [6]. Unfortunately, a sign error in Eq. (4) of that paper led to a corresponding sign error in the value of Π reported there.

The core ion properties deduced from these measurements are summarized in Table IX and compared with the values reported earlier in Ref. [6]. The quadrupole moment, Q, is determined with 0.02% precision and agrees well with the less precise value obtained in the optical RESIS study [6]. The hexadecapole moment, Π, is determined with 15% precision and also agrees well with the preliminary measurement after correcting the sign error in reference [6]. Both scalar and tensor dipole polarizabilities are determined more precisely than in reference [6], 0.03% and 1.3%, respectively, and are in satisfactory agreement with the earlier report. The scalar quadrupole polarizability, determined to 15% with partial reliance on theoretical calculations [14], is reported here. The vector hyperpolarizability, $\beta_{D,1}$, is reported, and its precision, 5%, is considerably better than that of the measurements of this quantity in Ar^+ and Ne^+ reported in Ref. [11]. The magnetic dipole moment, or g value, is determined to 1.1%. It differs from the Lande value (6/5) by 4.5(1.1)%. This result is somewhat surprising since the ground state is thought to be a nearly pure $^2D_{5/2}$ level, but the data are insistent that $g \neq 6/5$ since that would require an intercept of 3.195×10^{-5} in Fig. 6. No evidence for a permanent magnetic octupole moment is found, although the method appears capable of resolving such a term if measurement precision could be improved.

Also shown in Table IX, when available, are theoretical calculations of the Ni^+ properties. Since the ground state of Ni^+ is a $3d^9\,^2D_{5/2}$ level, excited levels involve two holes in the $3d$ shell and a valence electron, making theoretical calculations of transition probabilities difficult. Calculations by Beck and collaborators are in fair agreement for Q and Π [16] and for $\alpha_{D,0}$, and $\alpha_{D,2}$ [17]. Because of the agreement between these calculations and the measured dipole polarizabilities, the calculations of Beck *et al.* were used to estimate the value of $\beta_{D,0}$ that is needed to extract a value of the quadrupole polarizability from the measurements [14] and to estimate the value of the off-diagonal tensor polarizability, $\alpha_{D,2}(\Delta J = 1)$, Eq. (70) in Ref. [7], that enters into the calculation of the $E^{[2]}$'s shown in the Appendix [18]. We know of no calculations of the other Ni^+ properties listed in Table IX, but they now could serve as interesting tests of calculation methods. A calculation of the g value for the Ni^+ ground level would be particularly interesting. If it does, indeed, differ from the Lande value significantly, this could indicate the need for more careful calculations of the ground-state wave function. If careful calculations do not find deviations from the Lande value, it may be that this discrepancy indicates a limitation of our model for including the magnetic interactions. It may be worth noting that the 1.3% measurement of the g value of Ar^+ in Ref. [11] showed no deviation from the Lande value.

IV. DISCUSSION

The nickel Rydberg levels reported here display a far more complex structure than has been seen in previous studies using the microwave/RESIS technique. Studies of Rydberg levels bound to positive ions with $J_c = 0$, Si^{2+} [19] and Th^{4+} [20] and $J_c = 1/2$, Ba^+ [21], Mg^+ [22], and Si^{3+} [23], display only scalar structure. Studies of Rydberg levels bound to positive ions with $J_c = 3/2$, Ne^+ [24] and Ar^+ [11], show scalar, vector, and second-rank tensor structure. This study of nickel Rydberg levels, where the core ion Ni^+ has $J_c = 5/2$, displays all of these plus third- and fourth-rank tensor

TABLE VII. Scaled values of the third-order tensor structure factors and the corresponding scaled radial expectation values.

L	A_3 (a.u.)	$\langle r^{-5}\rangle$ (a.u.)	$\langle r^{-8}\rangle$ (a.u.)	$A_3/\langle r^{-5}\rangle$	$\langle r^{-8}\rangle/\langle r^{-5}\rangle$
6	$-3.65(50) \times 10^{-10}$	5.2632×10^{-9}	4.2018×10^{-13}	−0.069(10)	7.9835×10^{-5}
7	$-3.2(26) \times 10^{-11}$	1.6081×10^{-9}	3.6926×10^{-14}	−0.020(16)	2.2962×10^{-5}
8	$1.5(14) \times 10^{-11}$	5.271×10^{-10}	3.3705×10^{-15}	0.029(27)	6.3948×10^{-6}

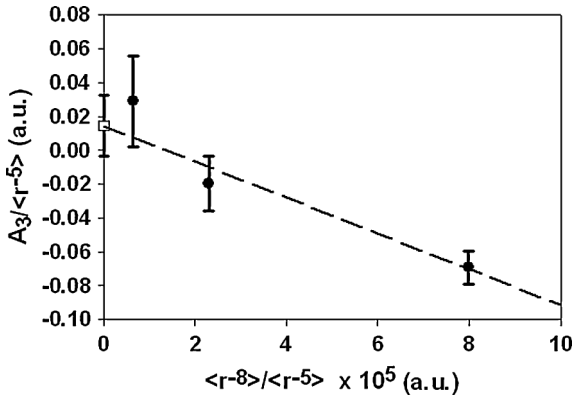

FIG. 8. Scaled values of the third-rank tensor structure factor, A_3, measured in the $n = 9$, $L = 6$, 7, 8 levels of the nickel atom. The coordinates are taken from Table VII. A nonzero intercept of this plot could indicate the value of the permanent magnetic octupole moment of the Ni^+ ion. The slope is related to a quantity called here the "octupole hyperpolarizability."

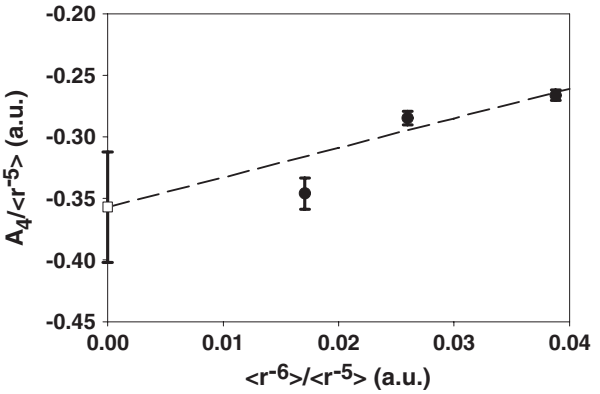

FIG. 9. Scaled values of the fourth-rank tensor structure factors describing the $n = 9$, $L = 6$, 7, 8 levels of nickel. The coordinates are taken from Table VIII. The extrapolated intercept is a measure of the permanent hexadecapole moment of the Ni^+ ion. Although the linear fit is poor, the intercept, marked by the open point, is clearly nonzero.

structure. As a result of this richer structure, more information about core properties can be deduced from the structure. All of these properties can, in principle, be calculated, but as Table IX illustrates, existing calculations are incomplete and only partially successful. Only one of the properties listed in Table IX is routinely measured for neutral atoms, the scalar polarizability $\alpha_{D,0}$, and even in that case, it is seldom measured to high precision. There are virtually no measurements of quadrupole moments of neutral atoms. One exception is the 6% measurement of the quadrupole moment of the ground state of Al by atomic beam methods [25]. Because of the importance of quadrupole interactions in atomic clocks based on trapped ions [5,26], there have been some recent measurements of ion quadrupole moments in excited states of clock ions motivated by this application [27–29]. Because both permanent and induced moments are important in many applications and because they are among the most direct descriptions of atomic behavior that depend on calculated wave functions, it is unfortunate that experimental measurements are so few and imprecise.

The fact that the measured structure in nickel conforms so well to the form expected from the effective potential model [7] is a confirmation of the assumptions of that model. The underlying physical assumptions are that the Rydberg system deviates only slightly from a zeroth-order picture consisting of a free core ion and a hydrogenic Rydberg electron and that the deviations that exist result exclusively from long-range interactions between the two. For sufficiently high-L Rydberg levels, the interactions between different Rydberg series are weak enough that the iterative scheme used here is practical. The energy shifts due to series interactions, $E^{[2]}$, are treated as corrections and applied before the remainder of the structure is fit to extract core parameters. Then, if necessary, the shifts $E^{[2]}$ are recalculated using the new values of the core parameters derived from the fits and the process iterated. An alternative approach, sharing the same physical assumptions, has been advanced by Greene and collaborators [15]. This approach, which is more appropriate if the interactions between Rydberg series are strong, includes these interactions from the outset and calculates a perturbed channel potential for every nL_K channel and then numerically calculates the binding energies of each Rydberg level within that channel. Both approaches have been used to analyze the structure of $n = 10$ Rydberg levels of Ne [15] and give comparable results for the inferred core properties. The approach used here is much simpler to apply, but it would be interesting to see the results of an alternative analysis. The level positions, reported in column 2 of Table II could be analyzed with the either method.

One advantage of the effective potential method [7] is that its relatively transparent derivation makes it easier to modify in situations where it is not directly applicable. A key assumption of the method is that excited levels of the core are well separated in energy from the ground state, allowing the adiabatic expansion to converge. If this is not the case the influence of low-lying core excited states, which contribute strongly nonadiabatic effects, must be dealt with separately. This is the case for another $J_c = 5/2$ ion studied with the optical RESIS method, the Fr-like Th^{3+} ion [30].

TABLE VIII. Scaled values of the fourth-order tensor structure factors and the corresponding scaled radial expectation values.

L	A_4 (a.u.)	$\langle r^{-5}\rangle$ (a.u.)	$\langle r^{-6}\rangle$ (a.u.)	$A_4/\langle r^{-5}\rangle$	$\langle r^{-6}\rangle/\langle r^{-5}\rangle$
6	$-1.401(23) \times 10^{-9}$	5.2632×10^{-9}	2.0421×10^{-10}	−0.2662(43)	0.038 800
7	$-4.578(90) \times 10^{-10}$	1.6081×10^{-9}	4.1771×10^{-11}	−0.2847(56)	0.025 975
8	$-1.823(67) \times 10^{-10}$	5.271×10^{-10}	9.010×10^{-12}	−0.346(13)	0.017 093

TABLE IX. Summary of Ni^+ properties deduced from the measurements reported here. All quantities are either dimensionless or in atomic units.

Property	This report	Reference [6]	Theory
Q	−0.469 78(9)	−0.474(2)	−0.493[b]
Π	+0.36(5)	0.33(21)[a]	0.204[b]
$\alpha_{D,0}$	7.949(2)	7.92(6)	7.9473[c], 7.7782[d]
$\alpha_{D,2}$	0.905(12)	1.15(14)	0.728[c], 0.962[d]
$\alpha_{Q,0}$	55(8)		
$\beta_{D,1}$	0.454(24)		
g_J	1.257(14)		
C_{M3}	0.014(18)		

[a]Due to a sign error in the last term of Eq. (4) in Ref. [6], the value of Π was reported there with the incorrect sign.
[b]Reference [16].
[c]Reference [17], method 1.
[d]Reference [17], method 2.

ACKNOWLEDGMENTS

This work was supported by the Chemical Sciences, Geosciences, and Biosciences Division of the Office of Basic Energy Sciences, Office of Science, US Department of Energy. Mark Lindsay contributed significantly to the early stages of the study, and Jed Orrison assisted in collection of some of the data.

APPENDIX

The energy shifts caused by mixing between different Rydberg series due to long-range interactions can be described as the action of $V_{\rm eff}$ in second order. The first few terms of $V_{\rm eff}$ are given by

$$V_{\rm eff} = -\frac{\alpha_{D,0}}{2r^4} - \left(\frac{Q}{r^3} + \frac{\alpha_{D,2}}{2r^4}\right) \frac{X^{[2]}(J_c) \bullet C^{[2]}(\hat{r})}{\begin{pmatrix} J_c & 2 & J_c \\ -J_c & 0 & J_c \end{pmatrix}} - \frac{\Pi}{r^5} \frac{X^{[4]}(J_c) \bullet C^{[4]}(\hat{r})}{\begin{pmatrix} J_c & 2 & J_c \\ -J_c & 0 & J_c \end{pmatrix}} + \cdots . \tag{A1}$$

The energy shift of a given Rydberg level $(^2D_{5/2})nL_K$ due to its coupling to other Rydberg states bound to either fine structure level of the ground electronic state, $^2D_{5/2}$, or $^2D_{3/2}$, can be written as

$$E^{[2]}(nL_K) = -\sum_{J_c,n'L'} \frac{\langle (^2D_{5/2})nL_K | V_{\rm eff} | (^2D_{J_c})n'L'_K \rangle \langle (^2D_{J_c})n'L'_K | V_{\rm eff} | (^2D_{5/2})nL_K \rangle}{\Delta E_{J_c} + E(n') - E(n)}, \tag{A2}$$

where the sum runs over all possible n' and L' and both values of J_c, 5/2 and 3/2, except that the initial state is excluded. The term ΔE_{Jc} in the denominator is zero if $J_c = 5/2$ and 1506.94 cm^{-1} if $J_c = 3/2$. $E(n)$ is the hydrogenic binding energies of Rydberg levels with principal quantum number n.

In general, the importance of different terms in the matrix element of $V_{\rm eff}$ decreases with inverse power of the Rydberg radial coordinate. Truncating $V_{\rm eff}$ after Eq. (A1) leads to terms in Eq. (A2) proportional to Q^2, with total power -6, $Q\alpha$, with total power -7, and either α^2 or $Q\Pi$ with total power -8. These are all shown separately in the table below. All the terms in Eq. (A1) are scalars and so satisfy the selection rule $\Delta K = 0$. The first term also satisfies $\Delta L = \Delta J_c = 0$. The second term satisfies $\Delta L = \Delta J_c = 0, \pm 2$, and the third term satisfies $\Delta L = \Delta J_c = 0, \pm 2, \pm 4$, although since it occurs only in combination with the second term in terms included, the $\Delta L = \pm 4$ matrix elements do not enter into the calculation. The core properties, Q, $\alpha_{D,2}$, and Π that can couple the two core fine structure levels have different values when they are diagonal and off-diagonal in J_c. In the case of Q and Π, these are inferred assuming LS coupling for the ground state. In the case of $\alpha_{D,2}$, the diagonal and off-diagonal tensor polarizabilities are different linear combinations of dipole matrix elements [7].

All of the relevant terms in Eq. (A2) can be reduced, after some angular momentum algebra to a linear combination of sums over Rydberg radial matrix elements,

$$f(nL; J_c, s, q) \equiv \sum_{n'} \frac{[nL|r^{-s}|n'L'][n'L'|r^{-q}|nL]}{\Delta E_{J_c} + E(n') - E(n)}, \tag{A3}$$

where the square brackets represent radial integrals and the n' summation implicitly includes both discrete and continuum radial functions. These sums can be carried out using the Dalgarno-Lewis method [31].

The values of the core properties used to compute the $E^{[2]}$ energy shifts of all 18 levels of this study are shown below. With the exception of $\alpha_{D,2}(J_c = 3/2)$, which was estimated from calculations, and did not produce significant shifts, all of these properties were the result of an iterative procedure that converged to stable results:

$$\begin{aligned} \alpha_{D,0} &= 7.949, \\ Q &= -0.46978, \quad Q(\Delta J_c = 1) = -0.23489, \\ \alpha_{D,2} &= 0.905, \quad \alpha_{D,2}(\Delta J_c = 1) = -0.04, \\ \Pi &= 0.36, \quad \Pi(\Delta J_c = 1) = 0.51. \end{aligned}$$

The partial contributions from each combination of terms in Eq. (A2) for each level are shown in Tables X–XII. The contribution labeled $\Delta n = 0$ represents the shift due to mixing with other $n = 9$ Rydberg levels with $\Delta L = \pm 2$. These are due only to the $(\alpha_{D,2})^2$ terms since the Q^2 terms are identically zero due to a property of hydrogenic radial functions.

TABLE X. Calculated values of the second-order energies in V_{eff} for the $n = 9$ Rydberg levels of nickel with $L = 6$. Each column corresponds to a specific combination of terms from Eq. (A2), as indicated. The total calculated energy shift, shown in the next-to-last column, also appears in Table II of the text. The uncertainty shown in the last column is estimated as half the total contribution from the columns $\alpha_{D,0}\alpha_{D,2}$, $\alpha_{D,2}\alpha_{D,2}$, $Q\Pi$, and $\Delta n = 0$. An additional uncertainty equal to half of the $\alpha_{D,0}\alpha_{D,0}$ contribution is later added to the scalar structure factor A_0. All values are in MHz.

K	J_c	QQ	$Q\alpha_{D,0}$	$\alpha_{D,0}\alpha_{D,0}$	$Q\alpha_{D,2}$	$\alpha_{D,0}\alpha_{D,2}$	$\alpha_{D,2}\alpha_{D,2}$	$Q\Pi$	$\Delta n = 0$	Total	σ_{conv}
3.5	2.5	−5.077	−8.809	−2.658	0.454	0.384	−0.010	0.000	0.214		
	1.5	7.493	0	0	0.062	0	0.001	0.077	0		
		2.416	**−8.809**	**−2.658**	**0.516**	**0.384**	**−0.009**	**0.077**	**0.214**	**−7.869**	**0.333**
4.5	2.5	6.348	−2.013	−2.658	−0.482	0.089	0.012	0.005	1.408		
	1.5	5.449	0	0	0.053	0	0.000	−0.129	0		
		11.797	**−2.013**	**−2.658**	**−0.429**	**0.089**	**0.012**	**−0.124**	**1.408**	**8.082**	**0.693**
5.5	2.5	6.803	3.524	−2.658	−0.530	−0.154	0.015	−0.036	0.563		
	1.5	3.073	0	0	0.030	0	0.000	0.060	0		
		9.876	**3.524**	**−2.658**	**−0.500**	**−0.154**	**0.015**	**0.024**	**0.563**	**10.690**	**0.224**
6.5	2.5	−0.554	6.142	−2.658	0.025	−0.268	0.003	.031	0.139		
	1.5	−0.288	0	0	−0.002	0	0.000	−0.003	0		
		−0.842	**6.142**	**−2.658**	**0.023**	**−0.268**	**0.003**	**0.028**	**0.139**	**2.567**	**0.219**
7.5	2.5	−7.854	3.877	−2.658	0.546	−0.170	−0.011	0.005	−0.077		
	1.5	−3.773	0	0	−0.024	0	0.000	0.001	0		
		−11.627	**3.877**	**−2.658**	**0.522**	**−0.170**	**−0.011**	**0.006**	**−0.077**	**−10.138**	**0.126**
8.5	2.5	−7.570	−5.537	−2.658	0.557	0.241	−0.011	−0.010	−0.005		
	1.5	−1.526	0	0	−0.009	0	0.000	−0.003	0		
		−9.096	**−5.537**	**−2.658**	**0.548**	**0.241**	**−0.011**	**−0.013**	**−0.005**	**−16.531**	**0.106**

TABLE XI. Calculated values of $E^{[2]}$ for nickel levels with $n = 9$, $L = 7$. All values in MHz.

K	Jc′	QQ	$Q\alpha_{D,0}$	$\alpha_{D,0}\alpha_{D,0}$	$Q\alpha_{D,2}$	$\alpha_{D,0}\alpha_{D,2}$	$\alpha_{D,2}\alpha_{D,2}$	$Q\Pi$	$\Delta n = 0$	Total	σ_{conv}
4.5	2.5	−1.537	−2.122	−0.448	0.096	0.063	−0.002	0.000	−0.065		
	1.5	8.948	0	0	0.038	0	0	0.027	0		
		7.411	**−2.122**	**−0.448**	**0.134**	**0.063**	**−0.002**	**0.027**	**−0.065**	**4.998**	**0.011**
5.5	2.5	2.590	−0.372	−0.448	−0.130	0.011	0.002	0.000	−0.146		
	1.5	9.116	0	0	0.039	0	0	−0.043	0		
		11.706	**−0.372**	**−0.448**	**−0.091**	**0.011**	**0.002**	**−0.043**	**−0.146**	**10.619**	**0.088**
6.5	2.5	2.493	0.967	−0.448	−0.122	−.029	0.002	−0.005	.245		
	1.5	4.621	0	0	.019	0	0	0.018	0		
		7.114	**0.967**	**−0.448**	**−0.103**	**−0.029**	**0.002**	**0.013**	**0.245**	**7.761**	**0.116**
7.5	2.5	−0.124	1.529	−0.448	0.015	−0.046	0	0.005	0.027		
	1.5	−0.101	0	0	0.000	0	0	0.000	0		
		−0.223	**1.529**	**−0.448**	**0.015**	**−0.046**	**0**	**0.005**	**0.027**	**0.859**	**0.007**
8.5	2.5	−2.443	0.893	−0.448	0.124	−0.026	−0.002	0.001	0.000		
	1.5	−0.898	0	0	−0.004	0	0	0.000	0		
		−3.341	**0.893**	**−0.448**	**0.120**	**−0.026**	**−0.002**	**0.001**	**0.000**	**−2.803**	**0.014**
9.5	2.5	−2.541	−1.419	−0.448	0.135	0.042	−0.002	−0.001	0.000		
	1.5	−0.483	0	0	−0.002	0	0	0.000	0		
		−3.024	**−1.419**	**−0.448**	**0.133**	**0.042**	**−0.002**	**−0.001**	**0.000**	**−4.719**	**0.020**

TABLE XII. Calculated values of $E^{[2]}$ for nickel levels with $n = 9$, $L = 8$. All values in MHz.

K	J_c'	QQ	$Q\alpha_{D,0}$	$\alpha_{D,0}\alpha_{D,0}$	$Q\alpha_{D,2}$	$\alpha_{D,0}\alpha_{D,2}$	$\alpha_{D,2}\alpha_{D,2}$	$Q\Pi$	$\Delta n = 0$	Total	σ_{conv}
5.5	2.5	−0.554	−0.589	−0.086	0.025	0.012	0	0.000	−0.005		
	1.5	−0.612	0	0	−0.002	0	0	0.000	0		
		−1.166	**−0.589**	**−0.086**	**0.023**	**0.012**	**0**	**0.000**	**−0.005**	**−1.811**	**0.004**
6.5	2.5	1.115	−0.078	−0.086	−0.037	0.002	0	0.000	−0.013		
	1.5	−0.797	0	0	−0.003	0	0	0.001	0		
		0.318	**−0.078**	**−0.086**	**−0.040**	**0.002**	**0**	**0.001**	**−0.013**	**0.104**	**0.005**
7.5	2.5	1.129	0.293	−0.086	−0.035	−0.006	0	−0.001	0.079		
	1.5	−0.369	0	0	−0.001	0	0	0.000	0		
		0.760	**0.293**	**−0.086**	**−0.036**	**−0.006**	**0**	**−0.001**	**0.079**	**1.003**	**0.004**
8.5	2.5	0.264	0.434	−0.086	−0.004	−0.009	0	0.001	0.005		
	1.5	−0.034	0	0	0	0	0	0.000	0		
		0.230	**0.434**	**−0.086**	**−0.004**	**−0.009**	**0**	**0.001**	**0.005**	**0.571**	**0.002**
9.5	2.5	−0.490	0.237	−0.086	0.019	−0.005	0	0.000	0.000		
	1.5	−0.236	0	0	−0.001	00	0	0.000	0.000		
		−0.726	**0.237**	**−0.086**	**0.018**	**−0.005**	**0**	**0.000**	**0.000**	**−0.562**	**0.003**
10.5	2.5	−0.723	−0.413	−0.086	0.029	0.009	0	0.000	0.000		
	1.5	−0.152	0	0	0	0	0	0.000	0.000		
		−0.875	**−0.413**	**−0.086**	**0.029**	**0.009**	**0**	**0.000**	**0.000**	**−1.336**	**0.005**

[1] S. R. Lundeen, in *Advances in Atomic, Molecular, and Optical Physics*, edited by P. R. Berman and C. C. Lin, Vol. 52 (Academic Press, New York, 2005), pp. 161–208.

[2] A. Derevianko, W. R. Johnson, M. S. Safronova, and J. F. Babb, Phys. Rev. Lett. **82**, 3589 (1999).

[3] J. Mitroy, M. S. Safronova, and C. W. Clark, J. Phys. B **43**, 202001 (2010).

[4] F. Real, V. Vallet, C. Clavaguera, and J. P. Dognon, Phys. Rev. A **78**, 052502 (2008).

[5] D. Jiang, B. Arora, and M. S. Safronova, Phys. Rev. A **78**, 022514 (2008).

[6] J. A. Keele, S. L. Woods, M. E. Hanni, S. R. Lundeen, and W. G. Sturrus, Phys. Rev. A **81**, 022506 (2010).

[7] Shannon L. Woods and S. R. Lundeen, Phys. Rev. A **85**, 042505 (2012).

[8] Shannon L. Woods, Ph.D. thesis, Colorado State University, 2012.

[9] Beam Imaging Solutions, Inc., Longmont, CO (www.beamimaging.com).

[10] F. J. Deck, E. A. Hessels, and S. R. Lundeen, Phys. Rev. A **48**, 4400 (1993).

[11] M. E. Hanni, J. A. Keele, S. R. Lundeen, and W. G. Sturrus, Phys. Rev. A **78**, 062510 (2008).

[12] P. W. Arcuni, E. A. Hessels, and S. R. Lundeen, Phys. Rev. A **41**, 3648 (1990).

[13] Kjell Bockasten, Phys. Rev. A **9**, 1087 (1974).

[14] Donald R. Beck (private communication); this estimate is based on the dipole oscillator strengths that led to the successful estimates of $\alpha_{D,0}$ and $\alpha_{D,2}$ in Ref. [14].

[15] W. Clark, C. H. Greene, and G. Miecznik, Phys. Rev. A **53**, 2248 (1996).

[16] Donald R. Beck, J. Phys. B **45**, 225002 (2012).

[17] Donald R. Beck and L. Pan, J. Phys. B **43**, 074009 (2010).

[18] Donald R. Beck (private communication); this estimate, $\alpha_{D,2}(\Delta J = 1) \sim -0.04(40)$ a.u., was based on the dipole oscillator strengths from Ref. [14] along with decomposition of the $3d^2 4p$ and $3d^2 4f$ levels into LS basis to clarify the sign of their contribution to $\alpha_{D,2}(\Delta J = 1)$.

[19] R. A. Komara, M. A. Gearba, C. W. Fehrenbach, and S. R. Lundeen, J. Phys. B **38**, S87 (2005).

[20] Julie A. Keele, S. R. Lundeen, and C. W. Fehrenbach, Phys. Rev. A **83**, 062509 (2011).

[21] E. L. Snow and S. R. Lundeen, Phys. Rev. A **76**, 052505 (2007).

[22] E. L. Snow and S. R. Lundeen, Phys. Rev. A **77**, 052501 (2008).

[23] R. A. Komara, M. A. Gearba, S. R. Lundeen, and C. W. Fehrenbach, Phys. Rev. A **67**, 062502 (2003).

[24] R. F. Ward, Jr., W. G. Sturrus, and S. R. Lundeen, Phys. Rev. A **53**, 113 (1996).

[25] J. R. P. Angel, P. G. H. Sandars, and G. K. Woodgate, J. Chem. Phys. **47**, 1552 (1967).

[26] W. M. Itano, Phys. Rev. A **73**, 022510 (2006).

[27] W. H. Oskay, W. M. Itano, and J. C. Bergquist, Phys. Rev. Lett. **94**, 163001 (2005).

[28] C. F. Roos *et al.*, Nature (London) **443**, 316 (2006).

[29] G. P. Barwood, H. S. Margolis, G. Huang, P. Gill, and H. A. Klein, Phys. Rev. Lett. **93**, 133001 (2004).

[30] J. A. Keele, M. E. Hanni, S. L. Woods, S. R. Lundeen, and C. W. Fehrenbach, Phys. Rev. A **83**, 062501 (2011).

[31] R. A. Komara, W. G. Sturrus, D. H. Pollack, and W. R. Cochran, Phys. Rev. A **59**, 251 (1999).